ACCSCIENCE PUBLISHING

International Journal of Bioprinting

RESEARCH ARTICLE

Design, mechanical validation, and clinical application of 3D-printed customized porous tantalum prostheses for total hip arthroplasty in fibrous dysplasia with shepherd's crook deformity

Hongyun Shao†, Jiawei Ying†, Qida Duan, Liangkun Sun, Fuyang Wang, Yong Wang, Pinqiao Yi, Bin Wu, Ning Luo, Qifan Yu, Liangliang Cheng*, and Dewei Zhao*

Department of Orthopaedics, Affiliated Zhongshan Hospital of Dalian University, Dalian, Liaoning, China

†These authors contributed equally to this work.

***Corresponding authors:**
Dewei Zhao
(zhaodewei2016@163.com)
Liangliang Cheng
(liangliang30766@163.com)

Citation: Shao H, Ying J, Duan Q, *et al*. Design, mechanical validation, and clinical application of 3D-printed customized porous tantalum prostheses for total hip arthroplasty in fibrous dysplasia with shepherd's crook deformity. *Int J Bioprint*. 2026:12(2):026090079.
doi: 10.36922/IJB026090079

Received: February 28, 2026

1st revised: April 2, 2026

2nd revised: April 18, 2026

Accepted: April 20, 2026

Published online: April 22, 2026

Abstract

For patients with fibrous dysplasia and severe "shepherd's crook" deformity, total hip arthroplasty presents substantial challenges because of complex anatomy, pathological bone changes, and prosthesis instability. This study reports an integrated clinical pathway encompassing digital virtual planning, three-dimensional (3D) printing customization, and biomechanical evaluation. Using the Mimics software, patient computed tomography data were reconstructed, and a biplanar oblique osteotomy below the greater trochanter was simulated to correct the deformity. An individualized cementless long-stem prosthesis was designed based on the corrected medullary canal, followed by topology optimization and construction of a 70% porosity biomimetic porous structure to induce bone ingrowth. Finite element analysis under 1,800 N axial load and ±10 N•m torque showed peak stresses of 183.7 MPa in the femoral stem and 316.92 MPa in locking screws, both below material yield limits. Interface micromotion ranged from 0.21 mm to 0.48 mm, within the 0.5 mm threshold for promoting bone ingrowth, confirming the superior stability of the 3D-printed customized porous tantalum prosthesis system. Clinical follow-up of two patients demonstrated improved Harris Hip Scores, with one case showing a stable prosthesis position without loosening or subsidence at five years postoperatively. These findings support the potential value of precisely tailored 3D-printed prostheses in managing complex femoral deformities and pathological bone defects.

Keywords: Fibrous dysplasia; Shepherd's crook deformity; 3D printing; Total hip arthroplasty; Porous tantalum; Finite element analysis

1. Introduction

Fibrous dysplasia (FD) is a rare benign bone disorder characterized by the replacement of normal bone tissue with fibrous tissue and immature woven bone, leading to significantly reduced mechanical strength, deformity, and a predisposition to pathological fractures.[1-4]

FD is clinically classified as monostotic or polyostotic and may occur as part of McCune–Albright syndrome.[5,6] The proximal femur is a major weight-bearing site and one of the regions most commonly affected by FD and prone to deformity, presenting as progressive coxa vara and femoral bowing, which can eventually progress to the classic "shepherd's crook" deformity.[7] This severe malalignment further leads to secondary hip osteoarthritis, causing patients to suffer from intractable pain and functional disability, severely impacting their quality of life.[8]

For FD patients with severe hip osteoarthritis or proximal femoral deformity, total hip arthroplasty (THA) has become an effective treatment option.[9] However, due to characteristics such as abnormal bone structure, osteopenia, widened medullary canals, and complex deformities in FD patients, traditional prostheses face significant challenges during implantation, including fixation difficulties, malalignment, and early loosening.[10] Early studies by Sierra and Cabanela[11] reported high rates of long-term prosthesis loosening and revision following THA in FD patients, particularly pronounced with the use of short-stem or cemented prostheses.

In recent years, with the advancement of digital orthopedics and three-dimensional (3D) printing technology, individually designed 3D-printed prostheses and surgical guides have demonstrated unique advantages in complex hip reconstruction. Yao *et al.*[12] first reported the application of 3D-assisted design in THA combined with long-stem cementless prostheses in FD patients, significantly improving surgical accuracy and prosthesis stability through precise preoperative planning of osteotomy schemes and prosthesis implantation pathways. However, research on the application and biomechanical evaluation of 3D-printed prostheses in treating FD with severe anatomical deformities remains scarce.

The present study reports two representative cases treated using 3D-printed customized prostheses for FD with severe femoral "shepherd's crook" deformity and proposes an integrated clinical pathway encompassing digital virtual planning, 3D printing customization, and biomechanical evaluation. This study seeks to explore the clinical value of this precise diagnostic and therapeutic approach in improving outcomes and functional reconstruction for patients with complex anatomical deformities.

2. Materials and methods

2.1. Clinical subjects and data collection

This study retrospectively analyzed two FD patients with severe proximal femoral deformities who underwent treatment with 3D-printed customized prostheses at the Affiliated Zhongshan Hospital of Dalian University, Liaoning, China. Both patients presented with typical "shepherd's crook" deformity and secondary hip osteoarthritis, and conservative treatment had failed. This study was approved by the Ethics Committee of the Affiliated Zhongshan Hospital of Dalian University (approval ID: 2022043). Written informed consent for treatment and use of clinical data/images for research and publication was obtained from both patients.

Patient data, including age, sex, symptoms, signs, and surgical history, were collected. Both patients underwent full-length anteroposterior X-rays of both lower limbs and computed tomography (CT) scans of the affected femur, and the Harris Hip Score (HHS) was assessed.

2.2. 3D-printed prosthesis design and fabrication

The workflow for fabricating the 3D-printed femoral prosthesis is illustrated in Figure 1**.** Initially, CT scan data of the patient's affected femur were extracted in DICOM format with a slice thickness of <1.5 mm. Subsequently, 3D image reconstruction was performed using Mimics 21.0 (The Materialise Group, Belgium), followed by a simulated biplanar oblique subtrochanteric osteotomy to anatomically correct the shepherd's crook deformity. Based on the corrected femoral morphology, a patient-specific cementless long-stem prosthesis was designed using SolidWorks 2021 (Dassault, France), featuring distal transverse locking screw holes to enhance rotational stability. In the fourth stage, topology optimization was performed using ANSYS Workbench 18.0 (ANSYS Inc., United States) to reduce implant mass and mitigate stress shielding while maintaining structural integrity. A biomimetic porous structure was then integrated onto the bone-contacting surfaces using nTopology 4.17.3 (nTopology Inc., United States) to promote osseointegration. Specifically, the porous region of the femoral stem was designed using a diamond lattice structure with a unit cell size of 2 mm and a porosity of 70%, yielding a pore size range of approximately 600–800 μm, which falls within the widely accepted range for promoting bone ingrowth (200–1,000 μm).[13,14] This level of porosity significantly reduces the elastic modulus of the prosthesis while preserving sufficient mechanical strength, achieving properties closer to those of human cortical bone, thereby effectively alleviating stress shielding and providing an ideal biomechanical environment for osteotomy site healing and long-term prosthetic stability. Previous studies have also indicated that a porosity range of 50–80% represents a common balance between osteointegration capacity and mechanical safety for porous orthopedic implants.[15-17] The final model was exported in STL format. Finally, the supporting structures and printing toolpaths were optimized using Magics. The prosthesis

was fabricated from medical-grade tantalum powder using selective laser melting technology with a precision of 0.1 mm. The fabrication parameters were consistent with those optimized in our previous studies[18]: the printing system was a Renishaw AM400 selective laser melting system (Renishaw plc, United Kingdom), and the material used was spherical tantalum powder (purity > 99.95 wt%; Stardust Technology Co., Ltd., China), prepared via inductively coupled plasma spheroidization, with a particle size range of 15–53 μm. The specific printing parameters were as follows: a laser power of 260 W, a laser spot spacing of 50 μm, an exposure time of 100 μs, a powder layer thickness of 30 μm, and a scan spacing of 65 μm. The printing process was performed on a high-purity tantalum substrate, with the equipment chamber filled with high-purity argon for protection, and the oxygen content was controlled below 0.1% to minimize the introduction of interstitial oxygen. Following production, vacuum heat treatment was performed to eliminate residual stress. The heat treatment parameters were as follows: heating rate of 10/min, holding temperature of 1,100, holding time of two hours, and vacuum level below 10^{-2} Pa, followed by furnace cooling to achieve optimal mechanical integrity.

2.3. Finite element analysis

This study utilized finite element analysis (FEA) to verify the biomechanical stability of the 3D-printed customized porous tantalum prosthesis after reconstructing the "shepherd's crook" deformity. To reduce computational complexity, the porous structure on the surface of the femoral stem prosthesis was simplified as solid geometry, and all threaded parts were simplified as smooth solid cylinders. The postoperative model of a representative case was imported into ANSYS Workbench 24.0 (Ansys Inc., United States). Tetrahedral meshing was performed using Solid186 elements. Mesh convergence verification was conducted to ensure mesh accuracy, using the equivalent stress in cortical and cancellous bone as the convergence criterion. Five mesh sizes—0.5, 1, 1.5, 2, and 3 mm—were selected for comparative analysis. The results showed that the difference in calculated results between the 1.5 mm mesh and the 0.5 mm and 1 mm meshes was less than 2%, indicating that the mesh had converged to a stable state. Considering computational cost, a mesh size of 1.5 mm, with 882,330 elements and 1,320,151 nodes, was ultimately adopted in this study.

Material properties are shown in Table 1.[18-20] The boundary conditions were configured based on typical loading conditions during walking for a 60 kg individual. Previous studies have indicated that during ground walking, the resultant force exerted by body weight combined with the muscles and ligaments around the hip can reach up to three times body weight.[21] Accordingly, a fixed support constraint was applied to the distal femur, and a 1,800 N vertical downward axial load was applied proximally on the prosthesis to simulate peak loading during single-leg stance or weight-bearing walking. Additionally, ±10 N·m internal or external rotation torque was applied to simulate torsional stress experienced by the femur during rotational activities such as turning.[22,23] Through these configurations, the biomechanical stability of the prosthesis under complex stress environments was systematically evaluated (Figure 2).

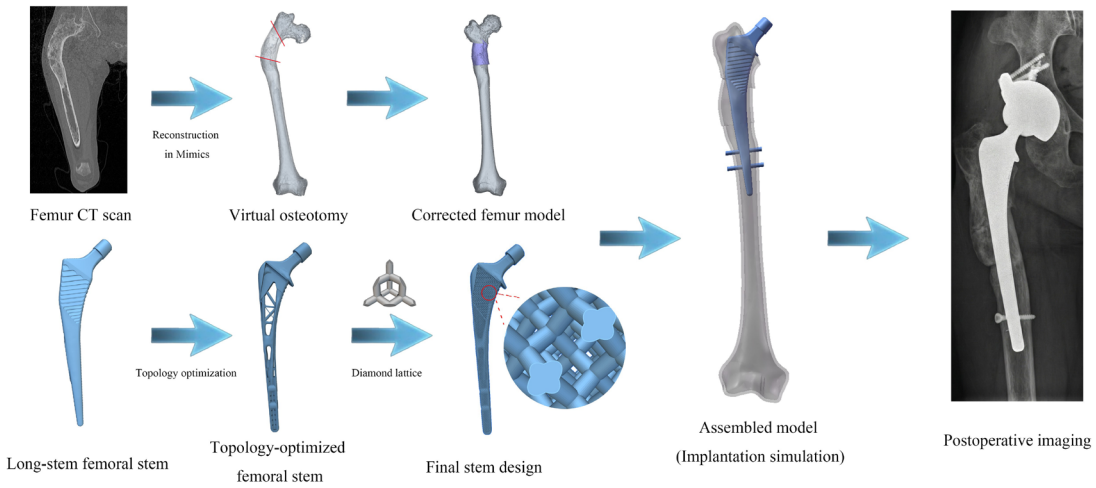

Figure 1. Design flowchart of the femoral stem prosthesis
Abbreviation: CT: Computed tomography.

Regarding contact settings, to realistically simulate postoperative initial stability, the interface between the proximal bone fragment and the prosthesis was set as a bonded constraint to simulate the mechanical characteristics of press-fit fixation. The interface between the mid and distal parts of the prosthesis and the femoral medullary canal was set as frictional contact with a friction coefficient of $\mu = 0.8$. The interfaces between locking screws and bone, and between screws and prosthesis, were both set as bonded to reflect their role as rigid internal fixation providing overall rotational support. Additionally, for the biplanar osteotomy site below the greater trochanter, frictional contact with a friction coefficient of $\mu = 0.3$ was set between the two opposing osteotomy surfaces to evaluate the micromotion and healing environment stability of the osteotomy site under functional loading.[19,24]

For finite element model validation, a conventional THA model was constructed for comparison by assuming bonded contact at the osteotomy site and removing the two distal locking screws, as this patient-specific reconstruction model has limited directly comparable validation data. Under identical loading and boundary conditions, the average principal strain (defined here as the strain with the maximum absolute value) was recorded at six predetermined points. These values were compared with those reported by Bieger *et al.*[25] to validate the accuracy of the finite element model, following a validation approach similar to that described by Liu *et al.*[26] The locations of the six measurement points were set according to the positioning of the strain gauges in Bieger *et al.*[25] and defined based on the Gruen zones, with measurement points 1 to 6 corresponding to zones 7, 6, 5, 1, 2, and 3, respectively (Figure 3A).

2.4. Surgery, postoperative management, and follow-up

All surgical procedures were performed by senior orthopedic surgeons according to standardized protocols. Under general anesthesia, patients were placed in the lateral decubitus position. The hip joint was exposed via an anterolateral approach, and intra-articular lesions were thoroughly debrided. After femoral neck base osteotomy and removal of the femoral head, the acetabulum was sequentially reamed and exposed. A 3D-printed porous tantalum acetabular cup was implanted, reinforced with screws, and a highly cross-linked polyethylene liner was inserted to complete the acetabular reconstruction. For femoral reconstruction, under the guidance of a 3D-printed surgical guide, precise biplanar osteotomy was performed to correct the deformity. Subsequently, the pre-made individualized 3D-printed femoral stem was implanted, and distal locking screws were accurately placed using an aiming device to enhance rotational stability. Intraoperative C-arm fluoroscopy and range-of-motion assessment were used to confirm alignment restoration and prosthesis stability (Figure 4).

Postoperatively, patients received routine prophylactic antibiotics and anticoagulation therapy. Rehabilitation commenced on the third postoperative day; patients were instructed to begin partial weight-bearing within two

Table 1. Material properties defined in the finite element models

Components	Materials	Elastic modulus (MPa)	Poisson's ratio (v)	Yield stress (MPa)	References
Cortical bone	Cortical bone	19,650	0.3	–	19
Cancellous bone	Cancellous bone	1,260	0.2	–	19
Locking screws	Titanium alloy	117,000	0.3	1,086	19
Femoral stem	Porous tantalum	8,963	0.31	420	18,20

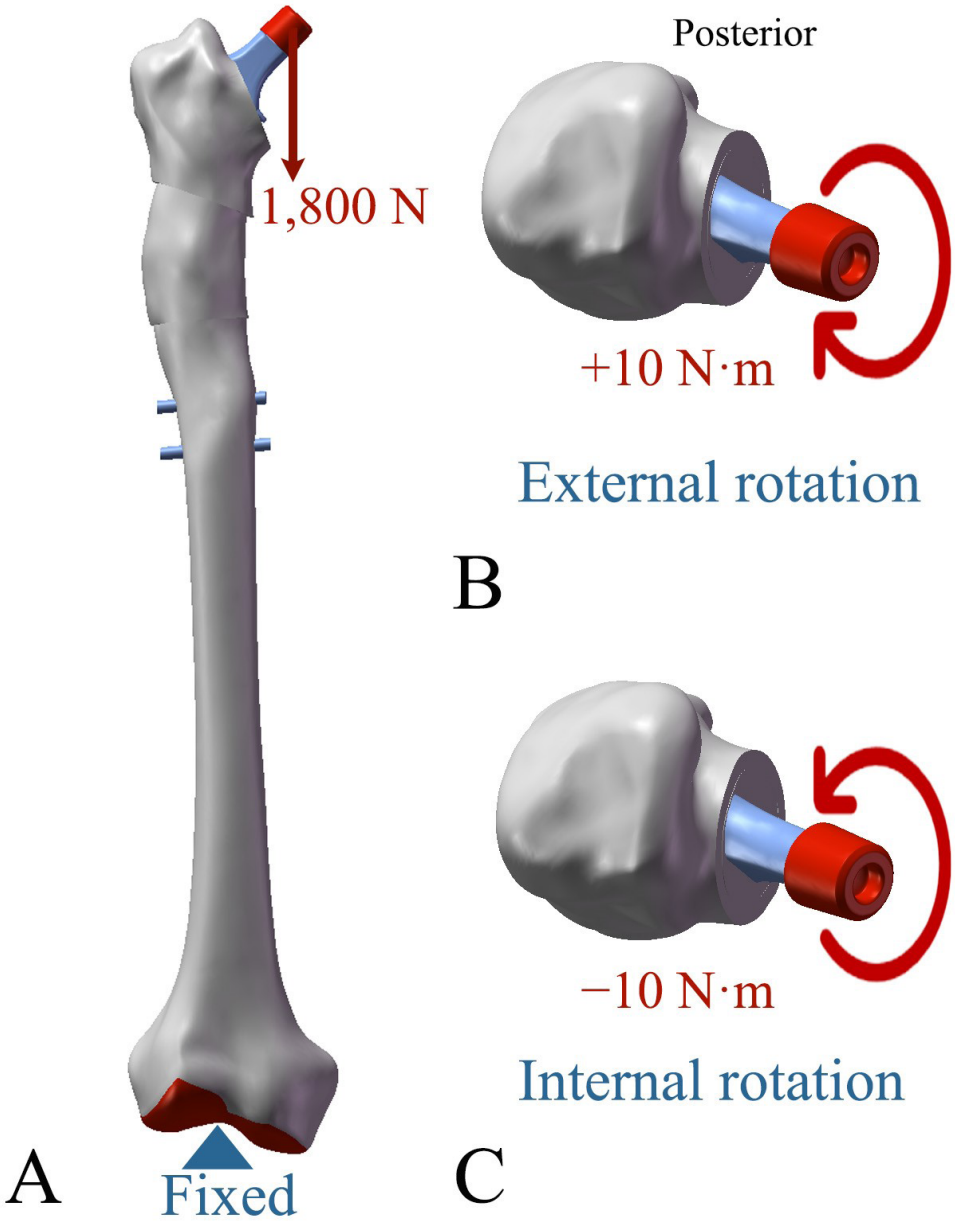

Figure 2. Loading and boundary conditions applied in the finite element analysis. (A) Vertical compression. (B) External rotation. (C) Internal rotation.

weeks after surgery and progress to full weight-bearing by approximately six weeks, as tolerated. Follow-up evaluations were conducted at 1, 3, 6, and 12 months post-surgery, and annually thereafter. Functional recovery was quantitatively assessed using the HHS, and healing progress at the osteotomy site, prosthesis position, and complications such as loosening or subsidence were dynamically observed using X-ray and CT imaging.

3. Results

3.1. Case reports

3.1.1. Case 1

A 56-year-old female presented with FD of the right proximal femur manifesting as a severe "shepherd's crook" deformity. The patient's primary symptom was persistent right hip pain exacerbated by weight-bearing,

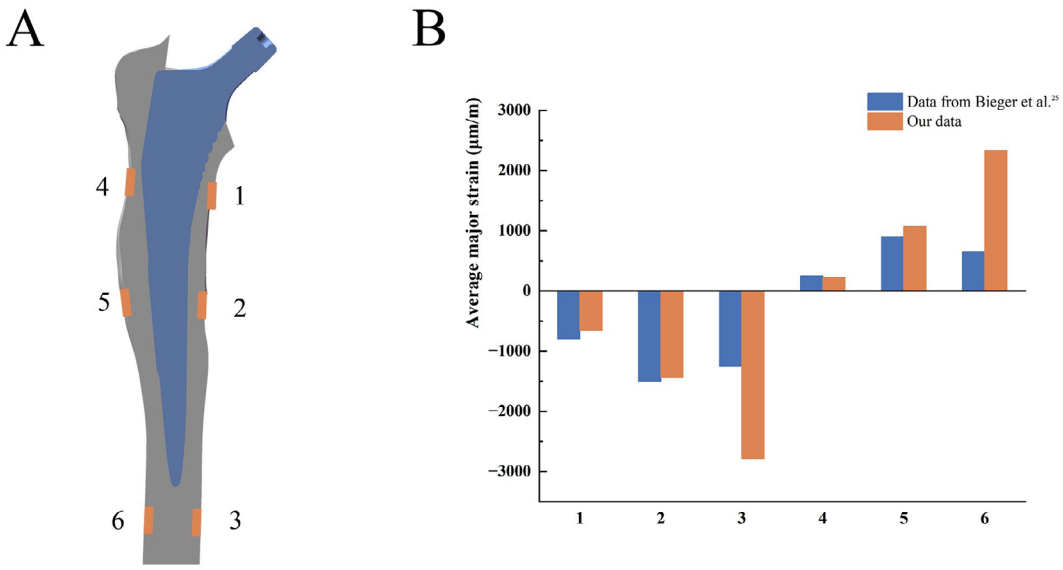

Figure 3. Validation of the finite element model. (A) Location of six measuring points on the medial and lateral sides of the femur. (B) Bar chart comparing strain measurements from this study and Bieger *et al.*[25] at the same measuring points.

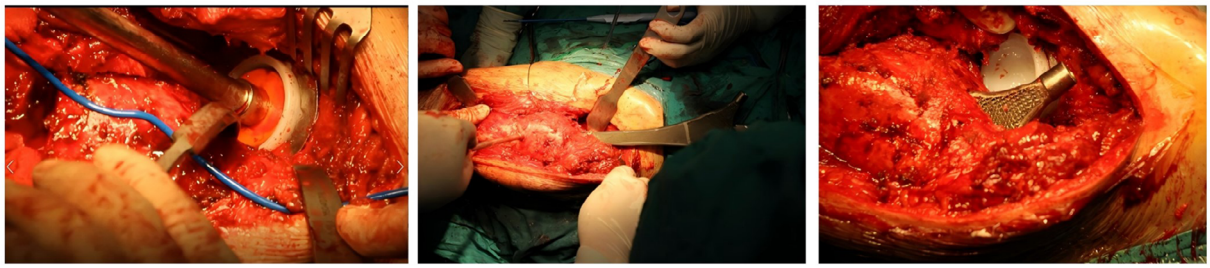

Figure 4. Surgical procedure

with the deformity contributing to a 4-cm limb-length discrepancy. The preoperative HHS was 40. Following the standardized process, osteotomy guided by a 3D-printed guide was performed intraoperatively, and a customized porous tantalum acetabular cup and femoral stem prosthesis were implanted. Intraoperative fluoroscopy confirmed that the final implant positioning was consistent with the preoperative digital simulation with respect to the restoration of limb length, neck-shaft angle, and anteversion, and the joint demonstrated excellent stability following reduction. At the 1-year postoperative follow-up, the HHS had significantly improved to 85, the limb shortening was successfully corrected, and the patient reported high satisfaction with her functional recovery. Radiographic evaluation revealed an absence of periprosthetic radiolucent lines, indicating stable biological fixation and effective osseointegration between the porous tantalum surface and the host bone (Figure 5).

3.1.2. Case 2

A 67-year-old male presented with FD of the left proximal femur and severe "shepherd's crook" deformity. Preoperatively, the patient had a typical limping gait, severe hip pain, limited mobility, and a 5-cm shortening of the left lower limb relative to the contralateral side. The preoperative HHS was only 35. The digitally planned biplanar osteotomy scheme precisely corrected the severe coxa vara deformity. The customized porous tantalum femoral stem prosthesis was successfully implanted intraoperatively, showing good proximal anatomical

fit, and the distal locking screws provided strong initial rotational support. At the final follow-up, five years postoperatively, imaging revealed complete bony union at the osteotomy site, satisfactory restoration of lower-limb alignment and length, and a stable prosthesis position without loosening, subsidence, or locking screw breakage. The HHS significantly improved from 35 preoperatively to 89, with the patient reporting no pain and good gait recovery (Figure 6).

3.2. Validation of the finite element model

The strain distribution predicted by the finite element model established in this study showed good agreement with the experimental measurements reported by Bieger *et al.*[25] Tensile strain was observed on the lateral side of the femur, while compressive strain was observed on the medial side. The strain values in the proximal femur at measurement points 1 and 4 were lower than those in other regions, and the strain magnitudes were similar to those reported by Bieger *et al.*[25] (Figure 3B), validating the accuracy and reliability of the present model. Notably, due to individual variations in femoral shaft size, medullary canal morphology, bone quality, femoral stem geometry, anteversion angle, and neck-shaft angle, certain differences existed in anatomical structure and prosthesis design between the present model and the experimental model used by Bieger *et al.*,[25] leading to slight discrepancies in local strain values within a reasonable range. Nevertheless, the consistency in the overall strain distribution pattern strongly supports the validity of the model.

3.3. Finite element analysis results

This study systematically evaluated the mechanical safety and initial stability of the 3D-printed customized system under complex mechanical environments through simulation of three typical physiological loads: standing, internal rotation, and external rotation.

In terms of stress distribution (Figure 7), under the combined loading of 1,800 N axial load and ±10 N·m torque, the individualized femoral stem prosthesis demonstrated excellent load-bearing capacity. The peak von Mises stress in the femoral stem occurred under the internal rotation condition, reaching 183.7 MPa, which accounted for only 43.7% of the yield strength of selective laser melting tantalum material (420 MPa), confirming a sufficient safety margin against plastic deformation.[18] The maximum von Mises stress experienced by the locking screws occurred under the standing condition, reaching 316.92 MPa, which is within the safe range of the yield limit for titanium alloy (1,086 MPa).[27] The maximum von Mises stress in the femur remained stable across the three conditions, fluctuating between 263.97 MPa and 319.69 MPa. Stress contour maps showed that stress peaks were mainly concentrated in the region of the distal osteotomy gap. This stress distribution pattern was effectively validated in clinical follow-up; imaging observation showed good bone healing progress on the medial side of the distal osteotomy gap, with no signs of bone resorption. According to Wolff's Law, the physiological stress stimulation maintained at the osteotomy site effectively promoted bone tissue healing.[28]

Regarding micromotion at the osteotomy site (Figure 8), the finite element results showed that the prosthesis system designed in this study exhibited excellent stability under all physiological conditions. Micromotion at the proximal interface was highly stable, ranging from only 0.21 mm to 0.23 mm across conditions. Micromotion at the distal interface was lowest under internal rotation (0.37 mm) and increased slightly under external rotation (0.48 mm). Previous studies indicate that the optimal micromotion range for promoting bone healing and inducing bone ingrowth should be within 0.5 mm.[29] All measured values were below this threshold, demonstrating the system's excellent resistance to rotation and shear forces. This stable mechanical environment not only effectively avoids the risk of fixation failure due to excessive micromotion but also creates ideal biological conditions for subsequent healing at the osteotomy site and bone ingrowth into the porous structure on the prosthesis surface.

4. Discussion

For patients with FD complicated by secondary hip osteoarthritis and "shepherd's crook" deformity, THA has become the preferred option for restoring joint function and alleviating pain. In this study, THA successfully relieved the patients' decades-long hip pain and effectively eliminated the mechanical pain caused by joint pathology. However, the severe anatomical deformity of the proximal femur, fragile bone biology, and abnormal biomechanical environment in such patients pose significant challenges for THA. The main challenges are precise correction of limb alignment and achievement of stable femoral fixation.

4.1. Precise alignment correction through the digital pathway

Limb alignment correction determines the patient's postoperative functional recovery. FD patients often present with coxa vara (decreased neck-shaft angle) and lateral bowing deformity of the femoral shaft. According to Pauwels' theory, coxa vara significantly increases shear force on the femoral neck and decreases compressive stress, leading to an increased risk of microfractures and impaired abductor muscle function.[30] For such deformities, valgus osteotomy is the fundamental method to restore the neck-shaft angle.[6,31,32] Closed-wedge valgus osteotomy at

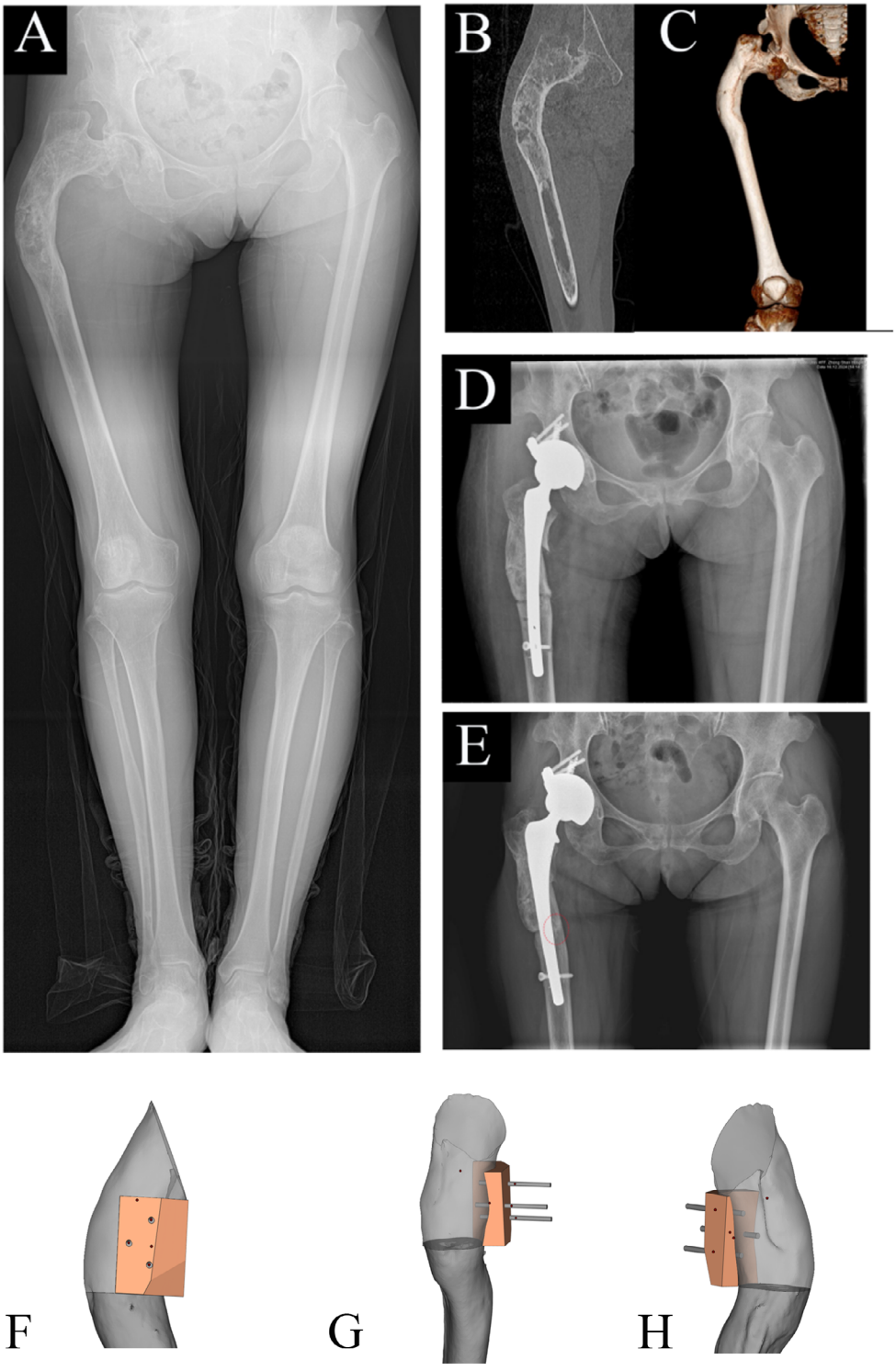

Figure 5. Imaging findings and osteotomy guide design for Case 1. (A) Preoperative X-ray. (B–C) Preoperative computed tomography images. (D) Immediate postoperative X-ray. (E) X-ray at 1-year follow-up. (F–H) 3D views of the osteotomy guide.

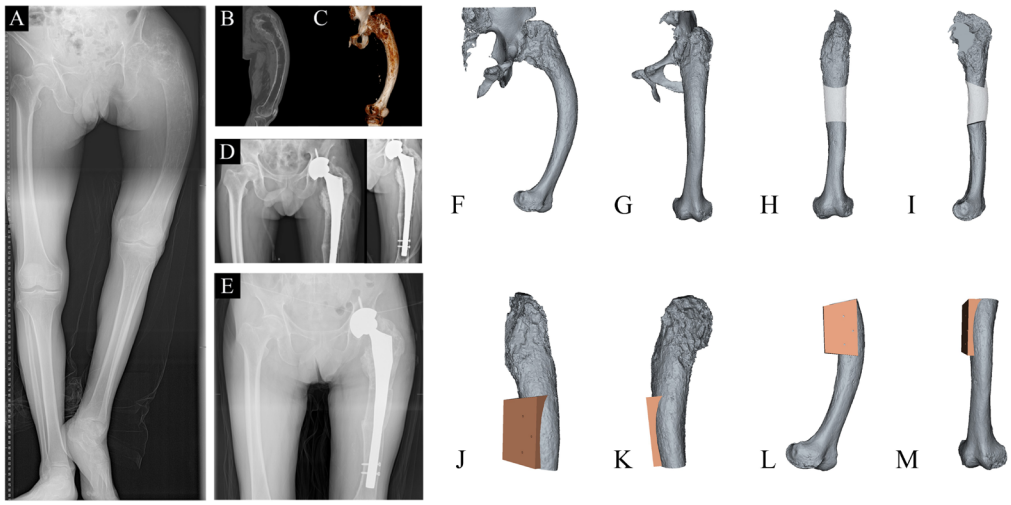

Figure 6. Imaging findings and osteotomy guide design for Case 2. (A) Preoperative X-ray. (B–C) Preoperative computed tomography images. (D) Immediate postoperative X-ray. (E) X-ray at 5-year follow-up. (F–I) 3D osteotomy simulation. (J–M) 3D views of the osteotomy guide.

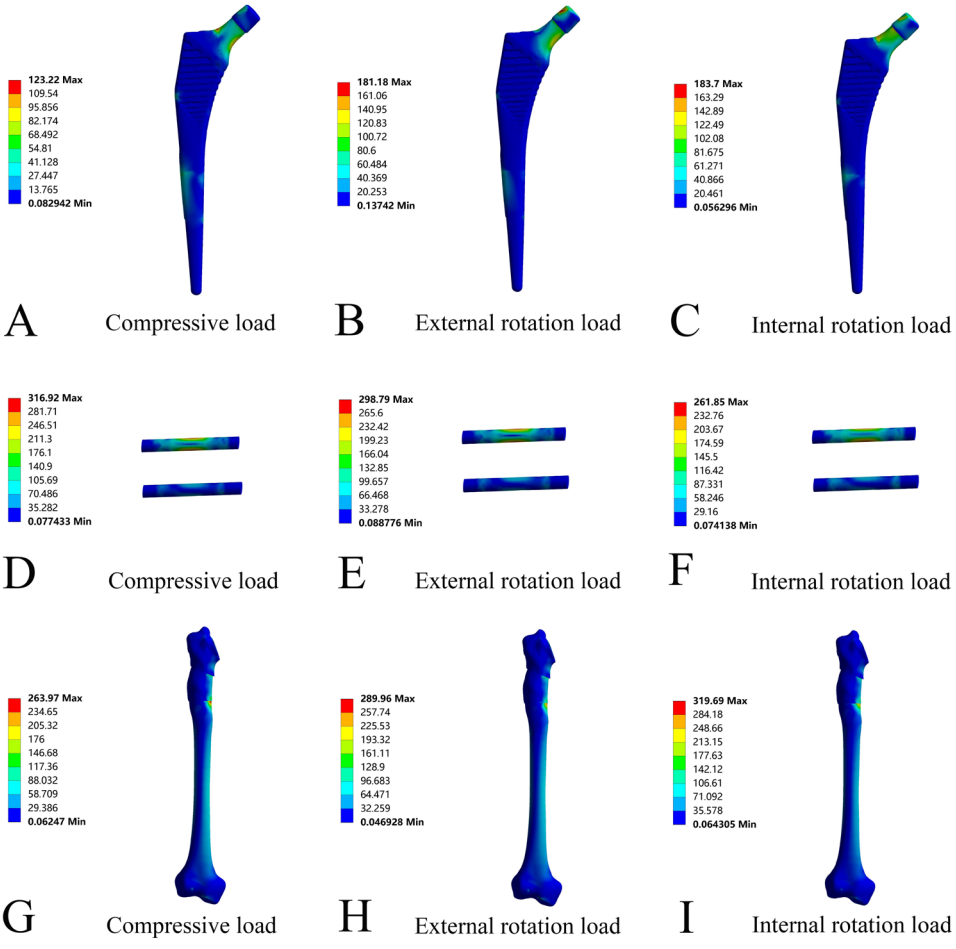

Figure 7. Finite element stress results. (A–C) Femoral stem. (D–F) Locking screws. (G–I) Femur.
Note: Unit of the legends: MPa.

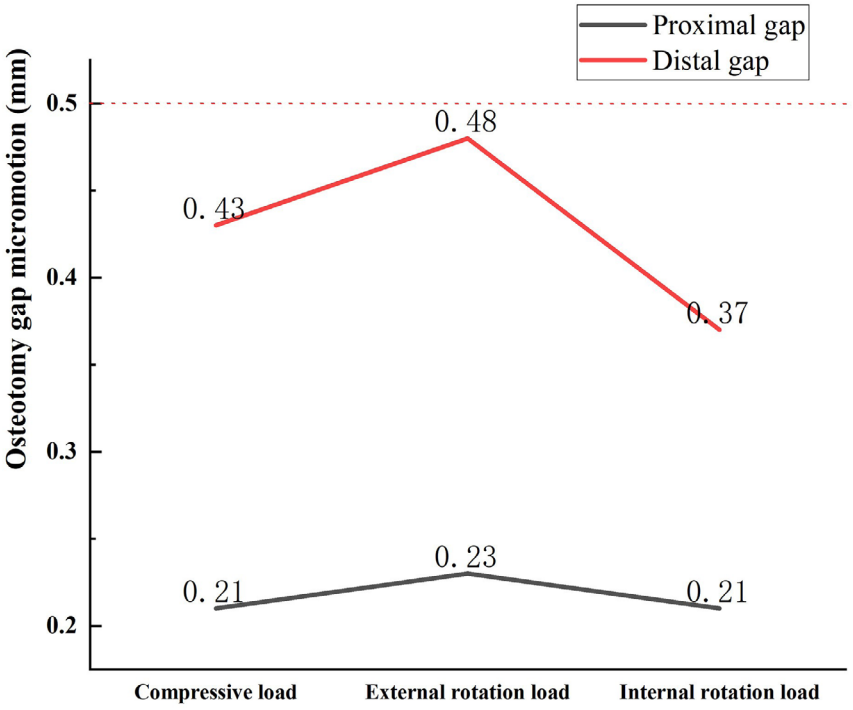

Figure 8. Finite element results for micromotion at the proximal and distal osteotomy gaps under the three loading conditions

the subtrochanteric level is commonly recommended.[33-35] Studies by Dheenadhayalan *et al.*[36] suggest proactive overcorrection (restoring the neck-shaft angle to 150–170°) to counteract the tendency for postoperative varus recurrence and improve the abductor muscle lever arm. In addition to proximal varus, lateral bowing deformity of the femoral shaft cannot be ignored. Ippolito *et al.*[37] pointed out that polyostotic FD is often accompanied by complex femoral coronal plane deformities. If the femoral shaft bowing is overlooked during surgery, abnormal stress will concentrate at the apex of the deformity. Dozo *et al.*[38] reported that this could lead to late periprosthetic stress fractures. Therefore, a second osteotomy at the apex of the femoral shaft bowing is also imporatnt to correct the lateral bow and restore femoral shaft aligment. This was fully reflected in the biplanar osteotomy design of our cases, aligning with the multi-site osteotomy strategies advocated by Zhang *et al.*[39] and Kandhari *et al.*[40]

This study utilized Mimics software for preoperative virtual planning, implementing a biplanar oblique osteotomy design below the greater trochanter, achieving precise correction of the lateral bowing deformity of the femoral shaft. Our digital pathway, guided by 3D-printed guides, enabled more accurate anatomical alignment, avoiding malalignment caused by empirical osteotomy. Clinical results showed marked correction of lateral bowing deformity and limb shortening in both cases.

4.2. Initial stability and mechanical validation of the prosthesis system

The stability of the femoral stem prosthesis is another core challenge for surgical success. Early studies by Sierra and Cabanela[11] indicated high rates of postoperative prosthesis loosening in FD patients, with early aseptic loosening rates for cementless prostheses reaching up to 60%, and cemented prostheses also posing long-term risks. With advancements in prosthesis design and surgical techniques, the current mainstream strategy favors the use of cementless tapered fluted long-stem prostheses, achieving press-fit fixation in the distal healthy diaphysis by bypassing the proximal diseased area. Garceau *et al.*,[9] using such prostheses, achieved very low rates of early loosening and revision in a mean 6-year follow-up. Moharrami *et al.*[41] also reported satisfactory radiological and functional outcomes in a patient with bilateral FD using long-stem prostheses at 1-year follow-up. Research by Jiang *et al.*[42] demonstrated that 3D-printed customized femoral stems could provide better medullary canal fit and significantly reduce micromotion, particularly suitable for patients with proximal femoral anatomical abnormalities.

The individualized long-stem prosthesis used in the present study, combined with distal locking technology,

achieves fixation in the distal diaphysis by bypassing the osteotomy site. To verify the rationality of this design, FEA was introduced. Under combined loading conditions, the peak stresses in the femoral stem (183.7 MPa) and locking screws (316.92 MPa) were far below the material yield limits, confirming that the topology-optimized design possesses sufficient mechanical strength while reducing weight.[18,27] Simultaneously, micromotion under all conditions was controlled between 0.21 mm and 0.48 mm, all within the 0.5 mm threshold conducive to bone ingrowth, providing a favorable bone healing environment.[29] For long-term biological fixation, the prosthesis surface features a biomimetic porous tantalum structure with 70% porosity, constructing an ideal interface for bone ingrowth.[13,14,43] Clinical follow-up results strongly support this; the stress distribution at the distal osteotomy site in Case 1 showed high spatial consistency with the clinically observed active bone healing area. Benefiting from the lower elastic modulus and excellent stress transmission characteristics of porous tantalum, the localized stress concentration at the osteotomy gap did not lead to stress shielding or interface failure, but rather acted as a physiological mechanical stimulus, effectively inducing bone tissue remodeling. Case 2, at the 5-year postoperative follow-up, showed complete healing of the osteotomy site and a stable prosthesis position, with the HHS significantly improving from 35 to 89. This fully demonstrates that the distal locking screws can function similarly to an interlocking intramedullary nail, providing a stable biomechanical environment for bone healing and functional reconstruction after correction.

4.3. Limitations and outlook

First, the finite element model in this study employed material parameters of normal cortical bone and did not fully simulate the heterogeneity of mechanical properties in bone tissue affected by FD. Given the heterogeneity of FD bone, accurately modeling individual pathological bone parameters remains challenging; the use of normal bone material parameters represents a limitation of the current model. Additionally, this study is limited by a small sample size ($n = 2$), which is attributable to the rarity of the disease and precludes formal statistical analysis. Nevertheless, the core value of this study lies in providing a systematic solution for the reconstruction of complex femoral deformities through a precise digital workflow. Future research will further advance FEA by incorporating mechanostat theory to evaluate bone modeling, along with fatigue simulation, to comprehensively validate prosthesis performance from multiple dimensions.[44] At the same time, larger-scale prospective studies combined with multi-center follow-up data are still needed to further refine the design specifications and clinical guidelines for 3D-printed prostheses in managing complex anatomical deformities.

In summary, this study demonstrates an effective pathway utilizing 3D printing technology to address the challenges of arthroplasty in FD with severe "shepherd's crook" deformity. Through precise preoperative virtual surgical planning, anatomical correction of lower limb alignment and deformity was successfully achieved. Relying on individualized topological design of the prosthesis and additive manufacturing technology, the biomechanical challenges of pathological medullary canal matching and initial fixation were effectively overcome. With the deep integration of materials science and digital orthopedic technology, this precise, individualized treatment strategy is gradually becoming an important development direction for managing complex anatomical deformities and joint functional reconstruction.

5. Conclusion

Through precise preoperative virtual planning and individualized prosthesis fitting, this approach successfully addresses the core challenges of lower limb alignment correction and prosthesis fixation. Finite element validation and follow-up results both indicate that the customized prosthesis system possesses sufficient strength, ensuring successful healing at the osteotomy site and long-term stability of the prosthesis. This precise and individualized diagnostic and therapeutic strategy provides an effective solution for joint reconstruction in cases with complex deformities and extreme bone conditions.

Acknowledgments

None.

Funding

This research was funded by the Dalian Dengfeng Plan Medical Key Specialty Construction Project (2021) (No. 243), the Dalian Science and Technology Innovation Fund (No. 2024ZDJH01PT140 and No. 2024RQ095), and the Liaoning Provincial Department of Education Basic Scientific Research Project Fund (No. LJ232511258004).

Conflict of interest

The authors declare no conflicts of interest.

Author contributions

Conceptualization: Liangliang Cheng, Dewei Zhao
Formal analysis: Fuyang Wang, Yong Wang, Pinqiao Yi
Investigation: Hongyun Shao, Qida Duan
Methodology: Jiawei Ying, Liangkun Sun
Writing–original draft: Hongyun Shao, Bin Wu, Ning Luo,

Qifan Yu

Writing–review & editing: Jiawei Ying, Liangliang Cheng, Dewei Zhao

Ethics approval and consent to participate

This study was approved by the Ethics Committee of the Affiliated Zhongshan Hospital of Dalian University (2022043). All procedures involving human participants were performed in accordance with institutional ethical standards. Written informed consent was obtained from all patients for participation.

Consent for publication

Written informed consent was obtained from all patients for participation, data usage, and publication of anonymized information and images.

Availability of data

Data will be made available from the corresponding author upon reasonable request.

References

1. Liu H, Fang X, Yu Z, Lang Y, Xiong Y, Duan H. Surgical strategy for benign lesions in proximal femur: Internal fixation or endoprosthetic replacement. *Int Orthop*. 2018;42(11):2691-2698.

   doi: 10.1007/s00264-018-3922-y

2. Wan J, Zhang C, Liu YP, He HB. Surgical treatment for shepherd's crook deformity in fibrous dysplasia: THERE IS NO BEST, ONLY BETTER. *Int Orthop*. 2019;43(3):719-726.

   doi: 10.1007/s00264-018-4074-9

3. Sauhta R, Makkar D. A closer look at fibrous dysplasia femur fracture five-year follow-up: A unique case. *J Orthop Case Rep*. 2024;14(2):155-159.

   doi: 10.13107/jocr.2024.v14.i02.4254

4. Johnson JL, Jacquez EA, Anderson JS, Adams BW. Surgical management of fibrous dysplasia and associated syndromes. *J Am Acad Orthop Surg*. 2025;33(15):e833-e840.

   doi: 10.5435/JAAOS-D-24-00717

5. Liu R, Tong L, Wu H, *et al*. Osteofibrous dysplasia: a narrative review. *J Orthop Surg Res*. 2024;19(1):204.

   doi: 10.1186/s13018-024-04682-3

6. Giles SN, Fernandes JA, Hampton MJ, Weston-Simmons S. Deformity correction, surgical stabilisation and limb length equalisation in patients with fibrous dysplasia: A 20-year experience. *Strateg Trauma Limb Reconstr*. 2021;16(1):41-45.

   doi: 10.5005/jp-journals-10080-1523

7. Jamshidi K, Bagherifard A, Hamidzadah Khiavi A, Mirzaei A. One-stage surgical correction of shepherd's crook deformity in fibrous dysplasia using fibular strut allograft augmentation: A retrospective case-series. *Int Orthop*. 2025;49(9):2069-2075.

   doi: 10.1007/s00264-025-06627-9

8. Kim HS, Im SB, Han I. Osteoarthritis of the hip in fibrous dysplasia of the proximal femur. *Bone Joint J*. 2015;97-B(7):1007-1011.

   doi: 10.1302/0301-620X.97B7.35828

9. Garceau S, Warschawski Y, Safir O, Gross A, Wolfstadt J, Kuzyk P. Total hip arthroplasty in patients with fibrous dysplasia: A modern update. *Can J Surg*. 2020;63(3):E202-E207.

   doi: 10.1503/cjs.007219

10. Soveral Pereira T, Malheiro N, Gonçalves D, Rodrigues C, Gonçalves PJ. Surgical treatment of fibrous dysplasia in the proximal femur: A literature review. *Eur J Orthop Surg Traumatol*. 2025;35(1):52.

    doi: 10.1007/s00590-025-04271-y

11. Sierra RJ, Cabanela ME. Total hip arthroplasty in patients with underlying fibrous dysplasia. *Orthopedics*. 2009;32(5):320-325.

    doi: 10.3928/01477447-20090501-14

12. Yao K, Min L, Tang F, *et al*. First application of three-dimensional designing total hip arthroplasty with long uncemented stem for fibrous dysplasia patients combined with hip joint osteoarthritis. *BMC Musculoskelet Disord*. 2019;20(1):204.

    doi: 10.1186/s12891-019-2608-y

13. Jin J, Wang D, Qian H, *et al*. Precision pore structure optimization of additive manufacturing porous tantalum scaffolds for bone regeneration: A proof-of-concept study. *Biomaterials*. 2025;313:122756.

    doi: 10.1016/j.biomaterials.2024.122756

14. Wang X, Zhang D, Peng H, Yang J, Li Y, Xu J. Optimize the pore size-pore distribution-pore geometry-porosity of 3D-printed porous tantalum to obtain optimal critical bone defect repair capability. *Biomater Adv*. 2023;154:213638.

    doi: 10.1016/j.bioadv.2023.213638

15. Jiao J, Hong Q, Zhang D, *et al*. Influence of porosity on osteogenesis, bone growth and osteointegration in trabecular tantalum scaffolds fabricated by additive manufacturing. *Front Bioeng Biotechnol*. 2023;11:1117954.

    doi: 10.3389/fbioe.2023.1117954

16. Yu H, Xu M, Duan Q, *et al*. 3D-printed porous tantalum artificial bone scaffolds: Fabrication, properties, and applications. *Biomed Mater*. 2024;19(4):042002.

    doi: 10.1088/1748-605X/ad46d2

17. Hu X, Kenan S, Cheng M, Cai W, Huang W, Yan W.

3D-printed patient-customized artificial vertebral body for spinal reconstruction after total en bloc spondylectomy of complex multi-level spinal tumors. *Int J Bioprint*. 2022;8(3):576.

doi: 10.18063/ijb.v8i3.576

18. Zhao D, Cheng L, Lu F, *et al*. Design, fabrication and clinical characterization of additively manufactured tantalum hip joint prosthesis. *Regen Biomater*. 2024;11:rbae057.

doi: 10.1093/rb/rbae057

19. Wang F, Liu Y, Huo Y, *et al*. Biomechanical study of internal fixation methods for femoral neck fractures based on Pauwels angle. *Front Bioeng Biotechnol*. 2023;11:1143575.

doi: 10.3389/fbioe.2023.1143575

20. Liu Y, Wang F, Ying J, *et al*. Biomechanical analysis and clinical observation of 3D-printed acetabular prosthesis for the acetabular reconstruction of total hip arthroplasty in Crowe III hip dysplasia. *Front Bioeng Biotechnol*. 2023;11:1219745.

doi: 10.3389/fbioe.2023.1219745

21. Cha YH, Yoo JI, Hwang SY, *et al*. Biomechanical evaluation of internal fixation of Pauwels type III femoral neck fractures: A systematic review of various fixation methods. *Clin Orthop Surg*. 2019;11(1):1-14.

doi: 10.4055/cios.2019.11.1.1

22. Chen J, Chen J, Lu R, Liu Y, Huang J, Zhang C. Finite element analysis, biomechanics, and clinical advantages of percutaneous medial column screw reinforced locking plate in the treatment of complex distal femoral fractures. *Bone Joint Res*. 2026;15(1):73-87.

doi: 10.1302/2046-3758.151.BJR-2025-0128.R2

23. Guoqing Z, Junxin L, Xiaoyu Z, Yongsheng Z, Bai Y. The design and processing of a 3D-printed high-performance biological fixation plate. *Int J Bioprint*. 2023;9(2):658.

doi: 10.18063/ijb.v9i2.658

24. Mao S, Liu Y, Wang F, *et al*. Design and biomechanical analysis of patient-specific porous tantalum prostheses for knee joint revision surgery. *Int J Bioprint*. 2023;9(4):735.

doi: 10.18063/ijb.735

25. Bieger R, Ignatius A, Decking R, Claes L, Reichel H, Dürselen L. Primary stability and strain distribution of cementless hip stems as a function of implant design. *Clin Biomech*. 2012;27(2):158-164.

doi: 10.1016/j.clinbiomech.2011.08.004

26. Liu B, Wang H, Zhang M, *et al*. Capability of auxetic femoral stems to reduce stress shielding after total hip arthroplasty. *J Orthop Transl*. 2023;38:220-228.

doi: 10.1016/j.jot.2022.11.001

27. Fu G, Zhong G, Yang Z, Cheng S, Ma L, Zhang Y. Two cannulated screws provide sufficient biomechanical strength for prophylactic fixation in adult patients with an aggressive benign femoral neck lesion. *Front Bioeng Biotechnol*. 2022;10:891338.

doi: 10.3389/fbioe.2022.891338

28. Frost HM. Wolff's law and bone's structural adaptations to mechanical usage: An overview for clinicians. *Angle Orthod*. 1994;64(3):175-188.

doi: 10.1043/0003-3219(1994)064<0175:WLABSA>2.0.CO;2

29. Wolf S, Janousek A, Pfeil J, *et al*. The effects of external mechanical stimulation on the healing of diaphyseal osteotomies fixed by flexible external fixation. *Clin Biomech*. 1998;13(4-5):359-364.

doi: 10.1016/s0268-0033(98)00097-7

30. Bartonícek J. Pauwels' classification of femoral neck fractures: Correct interpretation of the original. *J Orthop Trauma*. 2001;15(5):358-360.

doi: 10.1097/00005131-200106000-00009

31. Pan Y, Chen Y. Greater trochanteric osteotomy and subtrochanteric osteotomy in primary/revision total hip arthroplasty. *Front Surg*. 2023;10:1103689.

doi: 10.3389/fsurg.2023.1103689

32. Gallazzi E, Morelli I, Peretti G, Zagra L. What is the impact of a previous femoral osteotomy on THA? A systematic review. *Clin Orthop Relat Res*. 2019;477(5):1176-1187.

doi: 10.1097/CORR.0000000000000659

33. Vyas A, Godara A, Kumar N, Singhal S, Bhattacherjee D. Fibrous dysplasia of proximal femur: A case report of treatment with single-stage valgus osteotomy with dynamic hip screw and fibular strut graft. *Cureus*. 2022;14(1):e21496.

doi: 10.7759/cureus.21496

34. Singh AK, Srivastava S, Arunav A, Kumar A, Kumar A, Kumar M. A case report of bilateral shepherd crook deformity of proximal femur in an adolescent managed by corrective osteotomy, double angle blade plate and bone graft. *J Orthop Case Rep*. 2025;15(3):111-114.

doi: 10.13107/jocr.2025.v15.i03.5352

35. Harshavardhan JKG, Uppalapati BR, Menon PG. A case of fibrous dysplasia with bilateral shepherd crook deformity treated with dynamic hip screw fixation. *J Orthop Case Rep*. 2018;8(5):33-37.

doi: 10.13107/jocr.2250-0685.1096

36. Dheenadhayalan J, Avinash M, Lakhani A, Rajasekaran S. Shepherd's crook deformity: how to set it straight. A five-step surgical guide. *J Orthop Surg (Hong Kong)*. 2019;27(1):2309499019834362.

doi: 10.1177/2309499019834362

37. Ippolito E, Farsetti P, Boyce AM, Corsi A, De Maio F, Collins

MT. Radiographic classification of coronal plane femoral deformities in polyostotic fibrous dysplasia. *Clin Orthop Relat Res*. 2014;472(5):1558-1567.

doi: 10.1007/s11999-013-3380-1

38. Dozo MA, Abrego MO, Comba F, Zanotti G, Buttaro MA, Slullitel PA. Late periprosthetic femoral stress fracture associated with extra-articular deformity in a patient with fibrous dysplasia: a case report. *JBJS Case Connect*. 2023;13(3):e23.00017.

    doi: 10.2106/JBJS.CC.23.00017

39. Zhang X, Chen C, Duan H, Tu C. Radiographic classification and treatment of fibrous dysplasia of the proximal femur: 227 femurs with a mean follow-up of 6 years. *J Orthop Surg Res*. 2015;10(1):153.

    doi: 10.1186/s13018-015-0313-6

40. Kandhari VK, Bava SS, Desai MM, Wade RN. Single stage treatment of non-union of transcervical neck femur fracture with shepherd crook deformity of proximal femur in a case of fibrous dysplasia using dynamic hip screw fixation. *J Orthop Case Rep*. 2015;5(7):41-44.

    doi: 10.13107/jocr.2250-0685.304

41. Moharrami A, Mirghaderi P, Moazen-Jamshidi MM, Hoseini Zare N, Sharifpour S, Mortazavi SMJ. Bilateral total hip arthroplasty in a case with fibrous dysplasia: A case report. *J Med Case Rep*. 2023;17(1):371.

    doi: 10.1186/s13256-023-04084-9

42. Jiang Z, Cheng R, Dimitriou D, Yang Y, Tsai TY, Wang L. The 3D-printed customized femoral short stem offers improved anatomical parameters restoration, fitness and biomechanical performance compared with traditional femoral stem. *Orthop Surg*. 2025;17(4):1220-1229.

    doi: 10.1111/os.70000

43. Yang J, Gao H, Zhang D, *et al*. Static compressive behavior and material failure mechanism of trabecular tantalum scaffolds fabricated by laser powder bed fusion-based additive manufacturing. *Int J Bioprint*. 2022;8(1):438.

    doi: 10.18063/ijb.v8i1.438

44. Mehboob A, Barsoum I, Mehboob H, Abu Al-Rub RK, Ouldyerou A. Topology optimization and biomechanical evaluation of bone plates for tibial bone fractures considering bone healing. *Virtual Phys Prototyp*. 2024;19(1):e2391475.

    doi: 10.1080/17452759.2024.2391475